

A comparison in hierarchies and architectures between submarine trunk versus tributary canyons and their evolution: A case study from northwestern South China Sea margin

Dongwei Li^{a,b,c}, Chenglin Gong^{a,b,*}, Ronald J. Steel^d, Yijie Zhu^{a,b}

^a State Key Laboratory of Petroleum Resources and Engineering, China University of Petroleum (Beijing), Beijing, 102249, China

^b College of Geosciences, China University of Petroleum (Beijing), Beijing, 102249, China

^c Division of Earth and Planetary Sciences, Graduate School of Science, Kyoto University, Kyoto, 606-8502, Japan

^d Department of Earth and Planetary Sciences, Jackson School of Geosciences, The University of Texas at Austin, Texas, 78712, USA

ARTICLE INFO

Editor: Dr Giorgio Basilici

Keywords:

Trunk and tributary canyons
Canyon head
Hierarchies
Sedimentary architectures
Evolution
Qiongdongnan Basin

ABSTRACT

Submarine canyons are important conduits for transporting sediment across continental margins and their canyon heads contribute to further understanding the shelf-to-canyon sedimentary dynamics. Limited attention has been given to describe the internal depositional architectures and their variations from the tributary to trunk canyons in the canyon head regions. High-resolution 3-D seismic data tied to well logs, cores, and grain-size data from the Central Submarine Canyon head developed during late Miocene in Qiongdongnan Basin are utilized to investigate the variation of the hierarchical framework and depositional architectures between tributary and trunk canyons. The results show that canyon head tributaries contain one type of stratigraphic surfaces (i.e., fourth-order erosion surface) and four types of depositional elements (i.e., thalweg sandy debrites, axial high net-to-gross turbidites, off-axial low net-to-gross turbidites, and bank failures). The trunk canyon, in contrast, are characterized by a more complex hierarchical and depositional style, and are distinguished from tributary canyons by the occurrence of internal levees and the fifth-order erosion surface, composed of multiple seismically resolvable incisions. The evolution of the canyon head suggests that tributary canyons at the canyon head erode downstream and converge into the previously developed trunk canyon under the control of paleo-topography, forming a dendritic structure in plan-view. Results from this paper contributes to a better understanding on hierarchical framework and depositional architectures of the submarine canyon head.

1. Introduction

As well documented in literatures, submarine canyons are the large-scale incisions and principal conduits for the transport of sediments from shallow-marine/shelf to the deep-marine environments (Shepard, 1981; Babonneau et al., 2002; Harris and Whiteway, 2011; Puig et al., 2014; Bernhardt and Schwanghart, 2025). They can extend for hundreds of kilometers and act as conduits of turbidity flows and repositories of continentally-derived coarse sediment in deep-marine environments, which make them important targets for hydrocarbon exploration and potentially important reservoirs for the sequestration of CO₂ and/or hazardous fluids (e.g., Normark and Carlson, 2003; Gong et al., 2011; Janocko et al., 2013; Baker et al., 2024). They deliver and trap vast amounts of continental sediments and organic carbon to form the largest

sediment accumulations on Earth, which make them important archives of palaeoenvironmental and paleoceanographic changes (e.g., Galy et al., 2007; Baker et al., 2024). Similar to rivers on land, submarine canyons are not only one of the most distinct and frequently described landscapes and bedforms in deep-marine settings, but also key drivers in shaping the seafloor along Earth's continental margins (Harris et al., 2014). Submarine canyons, therefore, have long attracted attention from academia and oil industry (e.g., Shepard, 1981; Normark and Carlson, 2003; Cronin et al., 2005; Harris and Whiteway, 2011; Puig et al., 2014; Fildani, 2017; Bernhardt and Schwanghart, 2025).

The canyon head, as the shallowest portion of the canyon, often consists of tributary and trunk canyons and exhibits a dendritic structure (García et al., 2006; Tubau et al., 2013; Bernhardt et al., 2015; Puig et al., 2017; Maier et al., 2018), which is similar to the tributary and

* Corresponding author at: State Key Laboratory of Petroleum Resources and Engineering, China University of Petroleum (Beijing), Beijing, 102249, China.
E-mail address: chenglingong@cup.edu.cn (C. Gong).

<https://doi.org/10.1016/j.sedgeo.2025.106985>

Received 13 July 2025; Received in revised form 12 October 2025; Accepted 15 October 2025

Available online 21 October 2025

0037-0738/© 2025 Elsevier B.V. All rights are reserved, including those for text and data mining, AI training, and similar technologies.

trunk channels in deepwater environment (e.g., The Northwest Atlantic Mid-Ocean Channel, [Klaucke et al., 1998](#)), or terrestrial environment ([Bruno et al., 2021](#)). Technological advances in seismic and bathymetric imaging, together with the increased access to core and well-log data, our understanding of morphologies, morphological evolution and corresponding geneses of canyon heads has been greatly enhanced ([García et al., 2006](#); [Bernhardt et al., 2015](#); [Puig et al., 2017](#); [Maier et al., 2018](#); [Smith et al., 2018](#)). For example, sea level-controlled tributary canyons display characteristics of wider and deeper morphologies than those controlled by sediment supply ([García et al., 2006](#)). Along the flow direction, the size of the drainage network exhibits a decreasing trend from tributary to trunk canyons ([Tubau et al., 2013](#)). However, despite the morphological analysis ([García et al., 2006](#); [Tubau et al., 2013](#); [Puig et al., 2017](#)), few studies have been conducted to describe the internal depositional architectures and their variations from the tributaries to post confluences, resulting into a limited understanding on the variation of hierarchical framework and depositional architectures between tributary and trunk canyons.

In this study, high-resolution 3-D seismic datasets combined with well-log, core, and grain-size data from the head of the Central Submarine Canyon in the Qiongdongnan Basin along the northwestern South China Sea margin are utilized: (1) to document architectures of both trunk and tributary canyons; (2) investigate the variation of the hierarchical framework and depositional architectures between them; (3) explore their evolution.

2. Geological setting

The study area is located in the Qiongdongnan Basin of the

northwestern South China Sea margin, which is one of the most important petroliferous basins and largest Cenozoic rift basins in the South China Sea ([Fig. 1](#)). The Qiongdongnan Basin is a NE-trending, Cenozoic rift basin, and covers an area of $8.4 \times 10^4 \text{ km}^2$ with water depth ranging from 100 to 2800 m ([Xie et al., 2008](#); [Huang et al., 2016](#)). It undergone a complex tectono-stratigraphic evolutionary history, divided into four main stages, including a *syn*-rift stage in the Eocene (54.0 to 33.9 Ma), a rift-subsidence stage during the Oligocene (33.9 to 23.0 Ma), a post-rifting subsidence stage from early to middle Miocene (23.0 to 10.5 Ma), and an accelerated subsidence stage from late Miocene to Quaternary (10.5 to 0 Ma) (e.g., [Xie et al., 2008](#); [Morley, 2016](#); [Sun et al., 2022](#); [Yang et al., 2024](#)) ([Fig. 2](#)). The stratigraphy and sedimentary fill of the Qiongdongnan Basin are divided into four main megasequences accordingly ([Fig. 2](#)).

The *syn*-rift megasequence of Qiongdongnan Basin is bounded at its base by a basin-wide unconformity T100 dated to 54.0 Ma, and includes the Lingtuo Formation, lacustrine-marsh systems ([Fig. 2](#)) ([Xie et al., 2008](#); [Huang et al., 2016](#); [Morley, 2016](#); [Yang et al., 2024](#)). The rift-subsidence megasequence is bounded at its base by a regional unconformity T80 dated to 33.9 Ma, includes Yacheng and Lingshui Formations, and is characterized by depositional environments from lacustrine or marsh to nearshore marine (i.e., land-sea transition environments) ([Fig. 2](#)) ([Xie et al., 2008](#); [Sun et al., 2022](#); [Yang et al., 2024](#)). The post-rift megasequence is bounded at its base by the breakup unconformity T60 dated to 23.0 Ma, is composed of Sanya and Meishan Formations, and gave rise to shallow- to deep-marine environments ([Xie et al., 2008](#); [Sun et al., 2022](#); [Yang et al., 2024](#)). The accelerated subsidence megasequence is bounded at its base by a regional unconformity T40 dated to 10.5 Ma ([Fig. 1B](#)), comprises Huangliu, Yinggehai, and Ledong

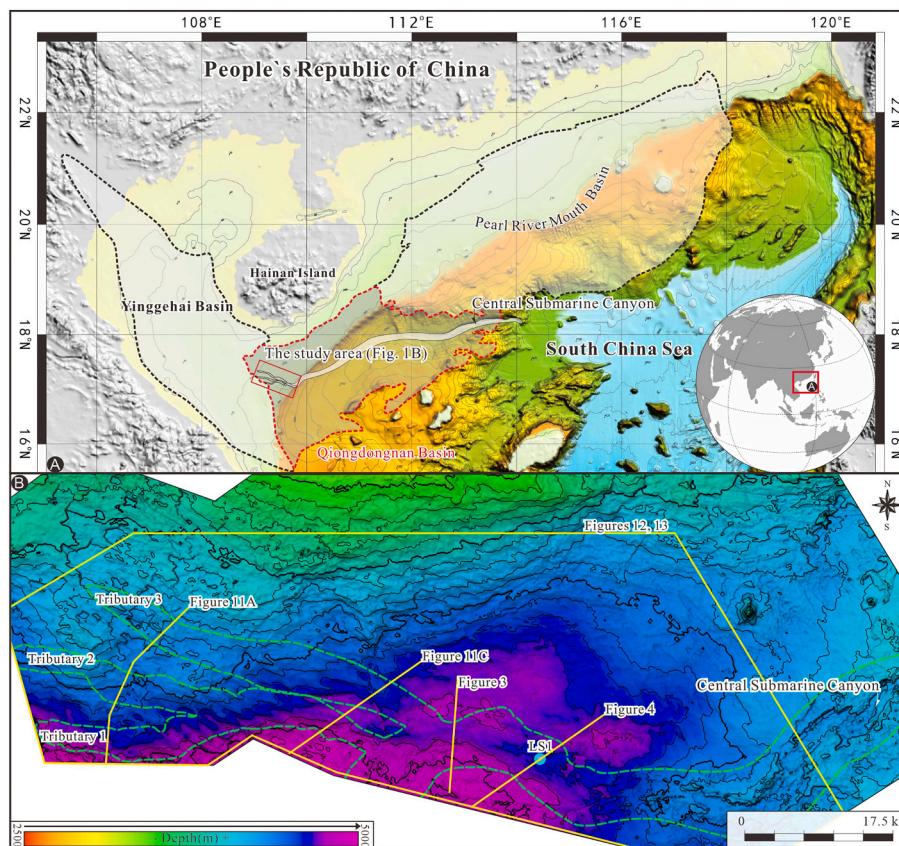


Fig. 1. (A) Bathymetric map showing the geographical location and context of the study area with respect to the Qiongdongnan Basin of the northwestern South China Sea margin (red polygon). (B) 3D perspective of the base of late Miocene Huangliu Formation (T40) showing the studied tributary and trunk canyons of the head of the Central Submarine Canyon. Also shown are plan-view locations of seismic lines and RMS amplitude maps shown in this study. Note that three tributary canyons downstream converge into the trunk canyon.

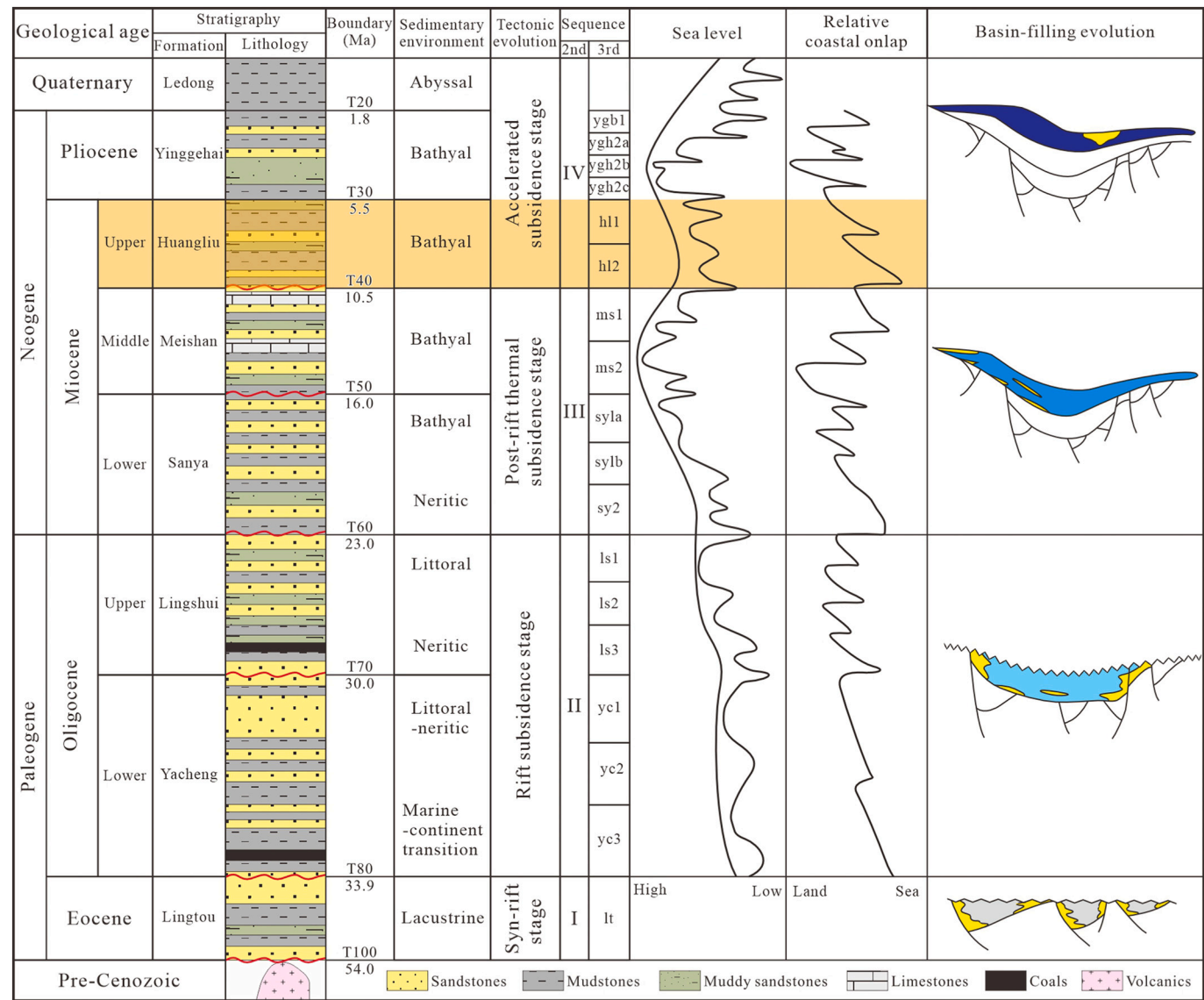


Fig. 2. Chronostratigraphic and tectono-stratigraphic column illustrating depositional and tectono-stratigraphic evolution history, sequence classification, and sea-level changes of the Qiongdongnan Basin, northwestern South China Sea (compiled from Sun et al., 2022; Yang et al., 2024). The orange rectangle highlights the studied stratigraphic interval of Central Submarine Canyon head.

Formations, formed in bathyal-abyssal environments and resultant deep-water systems (Xie et al., 2008; Gong et al., 2011; Sun et al., 2022; Yang et al., 2024).

Large-scale gravity-flow systems including submarine canyons, deepwater channels, submarine fans, and mass-transported complexes were formed in response to a more prominent shelf-slope-basin physiography from 10.5 Ma onwards, among which the Central Submarine Canyon of late Miocene age is regarded as one of the most distinctive landscapes (Fig. 1) (e.g., Xie et al., 2008; Gong et al., 2011). Variations of the hierarchical framework and depositional architectures between trunk and tributary canyons recognized in the head of the Central Submarine Canyon, and their evolution are the focus of the present research.

3. Datasets, methodologies, and terminologies

3.1. Datasets and methodologies

The datasets primarily used in this research consist of industry-standard depth migrated three-dimensional (3-D) seismic reflection

data and two exploration wells acquired by the China National Offshore Oil Corporation (CNOOC) from the head of the Central Submarine Canyon in the Qiongdongnan Basin of the northwestern South China Sea margin (Fig. 1). The seismic survey covers an area of ca. 2500 km², and have a sampling rate of 2 m, a bin size spacing of 25 (in-line) × 12.5 m (cross-line), and the seismic frequency bandwidth ranging from 10 to 40 Hz with a dominant frequency of 20 Hz (plan-view location of the seismic survey is shown in Fig. 1). They are displayed and interpreted in Halliburton Landmark software using the Society for Exploration Geophysicists (SEG) positive standard polarity, where a downward increase in acoustic impedance of a hydrocarbon reservoir base (i.e., a positive reflection coefficient) is represented by a central peak (plotted black). They are displayed using a red-white-black color bar, where the low-impedance hydrocarbon reservoir top is displayed as red seismic reflectors (Figs. 3 and 4). The 3-D seismic data (e.g., seismic profiles and RMS attributes) is tied to exploration well referred to as LS1 (plan-view location of this well is shown in Fig. 1B), containing lithologies based on cuttings, gamma-ray (GR) logs, sonic (DT) logs, density (DEN) logs, cores, and grain-size data (Figs. 5 to 8). Grain-size analysis was performed using the laser diffraction particle size analyzer Malvern

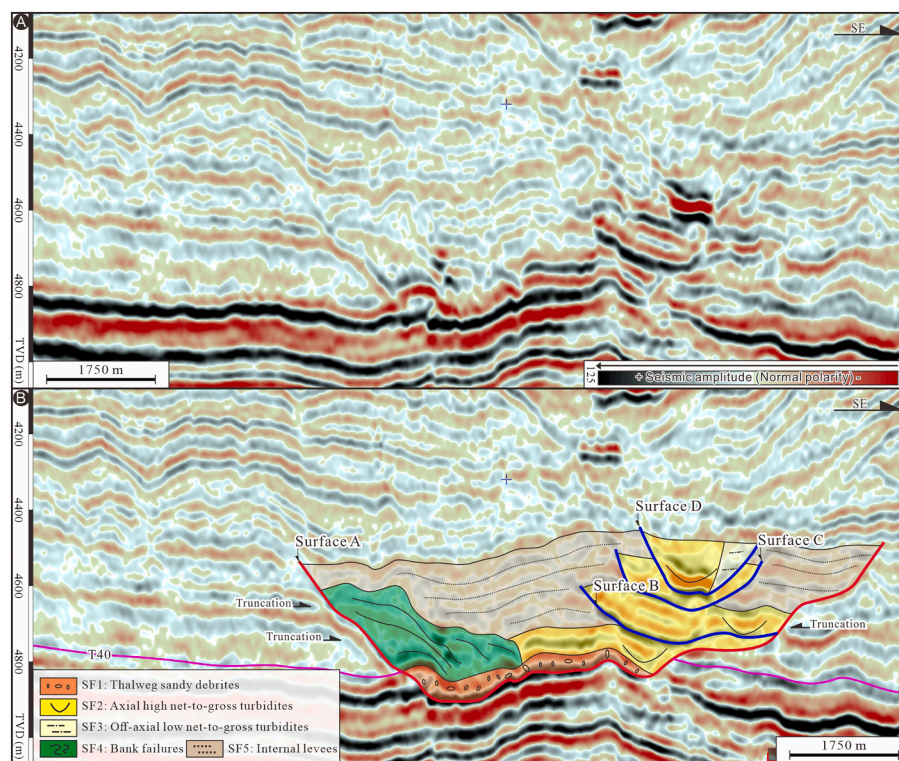


Fig. 3. Depositional strike-oriented seismic section across the studied trunk submarine canyon (see its plan-view location in Fig. 1B) and corresponding sedimentological interpretations illustrating hierarchies and architectures of the trunk canyon. Note that the trunk canyon contains two different types of stratigraphic surfaces and associated five main types of depositional facies. Also shown are stratigraphic position of RMS amplitude-attribute maps shown in Fig. 9. Surface A: fifth-order erosional surface (basal bounding surface of the trunk canyon); Surfaces B to D: fourth-order erosional surfaces; SF: seismic facies.

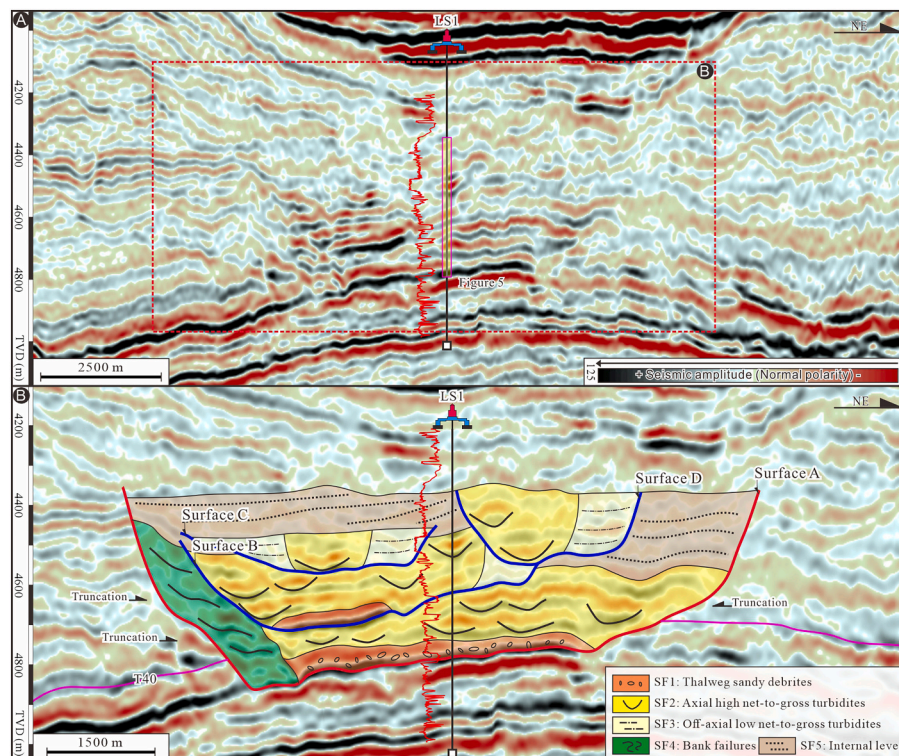


Fig. 4. Seismic-well tie transect across the studied submarine canyon (see its plan-view location in Fig. 1B) and associated sedimentological interpretations showing hierarchies and architectures of the trunk canyon. Also shown are stratigraphic position of the lithological and log-stratigraphic chart across well LS1 as shown in Fig. 5 and RMS amplitude-attribute maps shown in Fig. 9. Surface A: fifth-order erosional surface (basal bounding surface of the trunk canyon); Surfaces B to D: fourth-order erosional surfaces; SF: seismic facies.

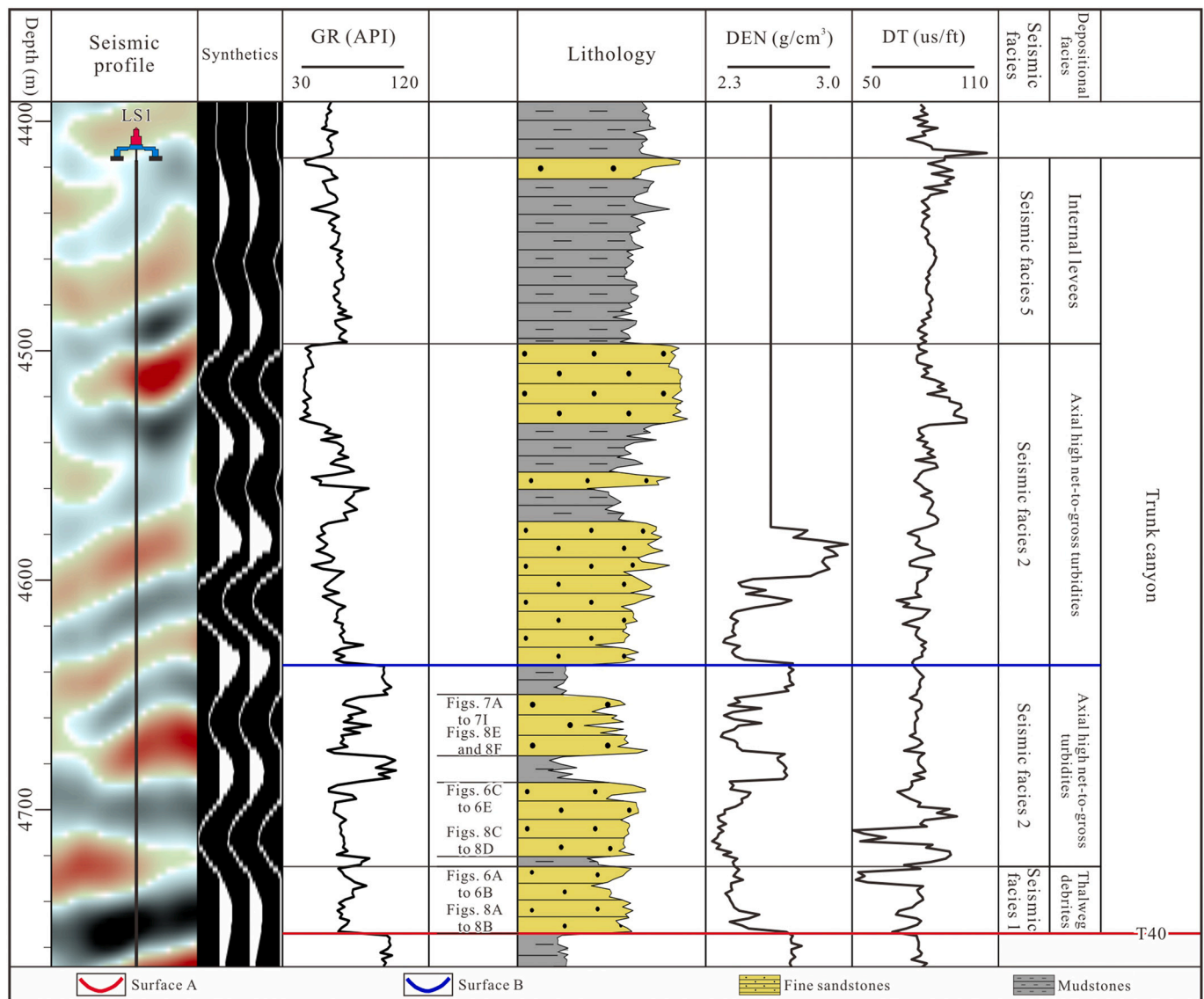


Fig. 5. Log-stratigraphic correlation and composite sections across well LS1 (see Figs. 1B and 4B for well locations) illustrating architectural properties of stratigraphic surfaces and depositional facies recognized in the trunk submarine canyon as penetrated by LS1. Refer to Fig. 4 for cross-sectional seismic manifestations of stratigraphic surfaces and sedimentary facies recognized in exploration well LS1. The irregular boundaries of lithology are GR logs. Also shown are stratigraphic positions of cores presented in Figs. 6 and 7. Surface A: fifth-order erosional surface (basal bounding surface of the trunk canyon); Surface D: fourth-order erosional surface.

Mastersizer 3000 at CNOOC Zhanjiang Experimental Center after removing the organic matter and carbonates by treatment with hydrogen peroxide (H₂O₂) and hydrochloric acid (HCL), and washing the samples with deionized water for 24 h until the pH became neutral. 19 samples from cores in well LS1 depth of 4640 to 4760 m were collected and examined for grain-size distribution patterns, and the effective particle size ranges from 2 to 0.004 mm (Fig. 8).

Seismic data interpretation of the documented submarine canyons was following the workflow proposed by Mayall and Kneller (2021), integrating 2-D seismic facies analysis (seismic stratigraphy) with a 3-D seismic geomorphology approach (i.e., RMS amplitude attributes). RMS attributes calculate the square root of the sum of the time-domain energy, offering an enhanced visualization of the stratigraphic architecture of small-scale depositional elements (Chopra and Marfurt, 2007), and yield more robust interpretations of lithology distribution and geologic process than section view-based seismic interpretations. Sedimentological analyses of the documented submarine canyons further including core observations and grain-size analysis. Cores with a total length of 20

m from well LS1 depth of 4640 to 4760 m were carefully observed and examined for sedimentary structures, grain-size variations, and vertical facies changes (Figs. 6 to 8).

3.2. Terminologies and hierarchical framework

Drawing on the hierarchical framework developed by Ghosh and Lowe (1993) from field data and Wonham et al. (2000) from seismic data for research on canyon fills, as well as the hierarchical framework proposed by Sprague et al. (2002, 2005) for understanding and predicting hydrocarbon-reservoir using subsurface data, we adopted a five-order hierarchical framework in current research. These hierarchical frameworks have been successfully used in other ancient gravity-induced deposits (Flint et al., 2011; Gong et al., 2021) and canyon fills (Anderson et al., 2006; Di Celma et al., 2010; Di Celma, 2011) worldwide. In current research, the erosion surfaces recognized in the Central Submarine Canyon head could be interpreted using a fifth-order hierarchical framework.

Core	Core sketch	Core description	Interpretation	Core	Core sketch	Core description	Interpretation
LF1		Gray, medium to coarse sandstones with fine pebbles and plant fossils	Sandy debris flows	LF2		Gray, massive medium to fine sandstones	High-density turbidity currents
LF1		Gray, medium to coarse sandstones with fine pebbles and plant fossils		LF2		Gray, massive medium to fine sandstones	
LF1		Gray, medium sandstones with fine pebbles and sharp lithological contacts	Mudstones	LF2		Gray, massive medium to fine sandstones	
LF1		Dark gray mudstones		LF2		Gray, massive medium to fine sandstones	
LF2		Gray, massive medium to fine sandstones	High-density turbidity currents	LF2		Gray, massive medium to fine sandstones	

Fig. 6. Core photographs and associated line drawings illustrating photographic facies details and sedimentological interpretations of thalweg sandy debrites composed of lithofacies 1 (LF1) (panels A and B) and axial high net-to-gross turbidites composed of lithofacies 2 (LF2) (panels C to E). The shown core photographs are from well LS1 at depth of 4687 to 4754 m. Please refer to Fig. 5 for the stratigraphic position of cores shown in this figure. G: fine pebbles; F: plant fossils.

- (1) First-order erosion surfaces refer to local erosional scours bounding a body of sediments with a fining-upward succession, which is typically recognizable in outcrop and core data (Ghosh and Lowe, 1993), and likely correspond to the basal surfaces of channel story (Sprague et al., 2002, 2005; Gong et al., 2021).

(2) Second-order erosion surfaces record an individual downcutting and filling succession of turbidites with a thickness up to several meters (Ghosh and Lowe, 1993; Di Celma, 2011). It is typically recognizable in outcrop and core data, is generally not possible to map seismically, and likely corresponds to the base of channel fill in the sense of Sprague et al. (2002, 2005).

(3) Third-order erosion surfaces have a thickness up to one hundred meters, represent the erosional surfaces bounding a coherent package of channel fill deposits with a surface of abandonment at their top (Ghosh and Lowe, 1993; Wonham et al., 2000; Di Celma, 2011). It is typically recognizable in well-log and seismic data, records a single cycle of channel cutting, filling, avulsion, and abandonment, likely corresponds to the base of channel complex in the sense of Wonham et al. (2000) and Sprague et al. (2002, 2005).
- (4) Fourth-order erosion surfaces developed within the canyon basal boundary and could be regionally tracked using seismic data. The elements bounded by them have a maximum width of several kilometers and a maximum thickness of several hundred meters (Wonham et al., 2000). They are likely corresponding to the base of channel-complex set in the sense of Sprague et al. (2002, 2005), and corresponding to the best stratigraphic surfaces that can be mapped with a relatively high degree of confidence at the scale of the studied canyon head using seismic data.

(5) Fifth-order erosion surfaces represent the largest-scale erosional surface identifiable and traceable across seismic profiles, bounding all the sedimentary fills of the ancient canyon, with widths spanning tens of kilometers and thicknesses ranging from hundreds to thousands of meters (Wonham et al., 2000), likely corresponds to base of channel system in the sense of Sprague et al. (2002, 2005).


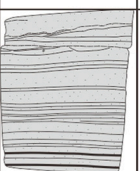



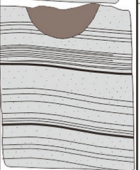

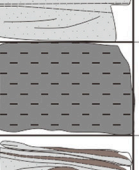



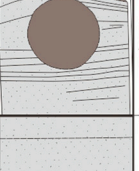
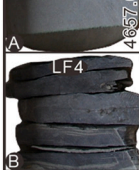
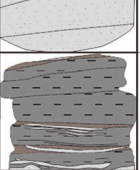


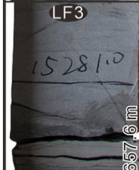
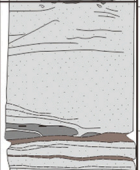
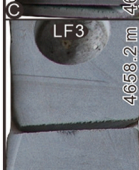
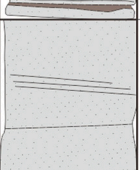

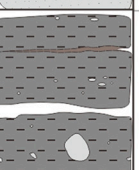


Core	Core sketch	Core description	Interpretation	Core	Core sketch	Core description	Interpretation
		Tb-Tc Gray, fine sandstones with parallel to low-angle bedding	Low-density turbidity currents			Tc Gray, fine sandstone with parallel to low-angle bedding and wavy bedding	Low-density turbidity currents
		Tb Gray, fine sandstones with parallel to low-angle bedding				Te Dark gray mudstones	Dilute turbidity currents
		Tb Gray, fine sandstones with low-angle bedding				Tb-Tc Gray, fine sandstones with parallel to low-angle bedding	Low-density turbidity currents
		Te Dark gray mudstones with nodules and capped sandstones	Dilute turbidity currents			Ta Gray, massive, medium to fine sandstones	High-density turbidity currents
		Tc Gray, medium to fine sandstones with low-angle bedding	Low-density turbidity currents				
		Td Gray, fine sandstones to siltstones	Low-density turbidity currents			Te Dark gray mudstones with nodules, sandy clumps	Dilute turbidity currents
		Tb-Tc Gray, fine sandstones with low-angle bedding					

Fig. 7. Core photographs and associated line drawings illustrating photographic facies details and sedimentological interpretations of axial high net-to-gross turbidites (LF2 to LF4). The shown core photographs are from well LS1 at depth of 4649 to 4676 m. Please refer to Fig. 5 for the stratigraphic position of cores shown in this figure. LF: Lithofacies.

4. Stratigraphic surfaces and depositional architectures within the studied canyon head

4.1. Description and interpretation of stratigraphic surfaces in the canyon head

Two types of stratigraphic surfaces (type 1 and type 2 shown in Figs. 3 to 5) are recognized in the studied canyon head, and are delineated and interpreted below:

Stratigraphic surfaces type 1 is the geometrically largest channel-shape surface developed at the base of the studied canyon, and separates canyon fills from the underlying deposits (red lines shown in Figs. 3 and 4). It is seismically recognized as a basal irregular erosional surface characterized by onlaps inside and truncations outside due to repeated channel erosion and complexity of lithological variations (Figs. 3 and 4). Stratigraphically, the surface type 1 appears as a sharp lithological contact, and corresponds to a sharp change from mudstones with high GR values nearly the shale baseline to sandstones with blocky well-log patterns of low gamma-ray responses (Fig. 5). It exhibits an overall U-shaped geometry, and is typically 5 to 10 km wide and 300 to 500 m

high (Figs. 3 and 4).

Stratigraphic surfaces type 2 shares great similarities in cross-sectional seismic appearance (i.e., U or V-shaped, basal irregular erosional surface with truncations below and onlaps above) and lithologic and well-log responses (i.e., sharp lithological contact with shift from mudstones with high GR values to sandstones with low GR values) with the above-mentioned stratigraphic surfaces type 1 (surfaces B to D shown in Figs. 3 and 4). It, in marked contrast, is in a stratigraphic scale below which erosional surfaces are not seismically traceable, and is therefore in a lower hierarchical level (Figs. 3 and 4). Besides, these surfaces exhibit cross-cutting relationships, causing earlier-formed surfaces being more difficult to fully preserved (Figs. 3 and 4). It is generally 3 to 5 km wide and 200 to 300 m high, and is therefore geometrically smaller than stratigraphic surfaces type 1 (Figs. 3 and 4).

The cross-sectional morphologies of both stratigraphic surfaces type 1 and type 2 (i.e., V or U-shaped, basal irregular erosional incisions cutting deeply into the underlying deposits) are interpreted as basal bounding surfaces of different hierarchical elements as described before (Wonham et al., 2000; Sprague et al., 2002, 2005; Di Celma, 2011). Among them, type 1 represents the largest erosional surface within the

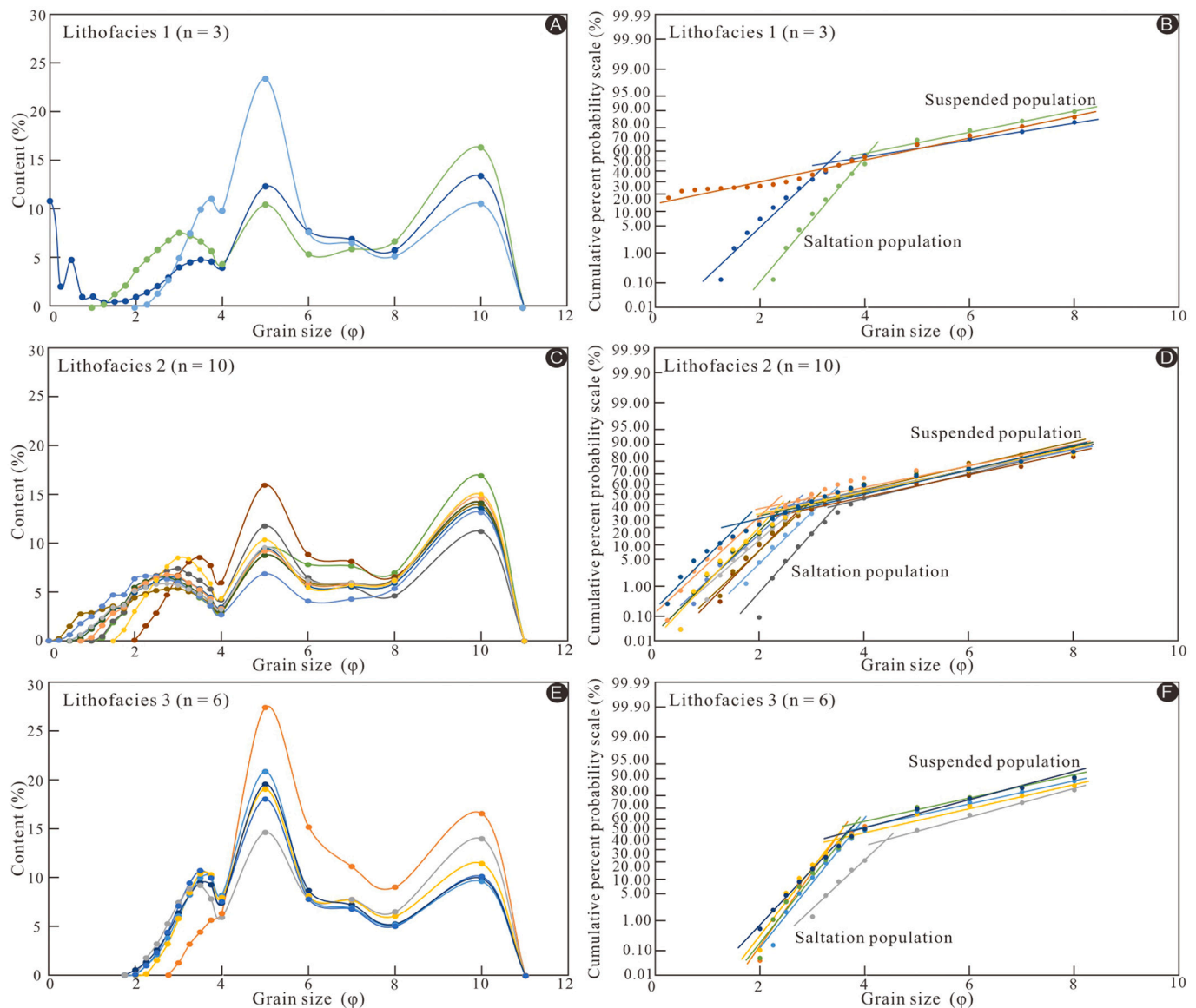


Fig. 8. Frequency distribution curves (left panels) and cumulative distribution diagrams (right panels) of thalweg sandy debrites (panels A and B) and axial high net-to-gross turbidites (panels C to F). The shown cumulative distribution and frequency distribution curves are based on 19 samples of cores from well LS1 at depth of 4649 to 4754 m (see their stratigraphic positions in Fig. 5). The X-axis coordinate is in logarithmic form.

studied canyon head, it delineates all the sedimentary deposits of the canyon (Figs. 3 and 4). In contrast, stratigraphic surfaces type 2 is smaller in both width and depth compared to type 1, all of the stratigraphic surfaces of type 2 were recognized and traced using seismic data within type 1 (Figs. 3 and 4), besides, it lacks internally developed erosional surfaces that can be traced using seismic data (Figs. 3 and 4). Those sedimentary infills delineated and separated by these surfaces were referred to as “channel-complex set” by other workers in those studies of submarine channels using seismic data (e.g., Sprague et al., 2002, 2005; Mayall and Kneller, 2021). Thus, we interpret stratigraphic surfaces type 1 (i.e., higher hierarchical level expressed as a cluster of multiple seismically traceable incisions) as the fifth-order erosion surface, and stratigraphic surfaces type 2 (i.e., lower hierarchical level expressed as a single seismically mappable incision) as the fourth-order erosion surface (Figs. 3 to 5).

4.2. Description and interpretation of seismic facies in the canyon head

Five seismic facies (seismic facies 1 to 5 in Figs. 3, 4 and in Table 1)

are recognized in the studied canyon head, they correspond to five different depositional facies, and are interpreted below. Among them, sedimentary interpretations for seismic facies 1, 2, and 5 derived from core and logging data, while seismic facies 3 and 4 were interpreted mainly through seismic facies analysis.

- (1) *Seismic facies 1 (continuous, low-frequency and high amplitude reflections)* exhibits blocky well-log patterns of low gamma-ray responses shown in well LS1 (Fig. 5). The lithofacies (Lithofacies 1) recognized in the cores from LS1 consists dominantly of 10 to 20 m thick, structureless, pebbly sandstones (with a sand content of 41.92 % - 55.54 %) with subordinate pebbles (Fig. 6A and B; Table 2). This lithofacies contains sharp lithological contacts from mudstones in the lower part and sandstones in the upper part (Fig. 6B), fine pebbles with the diameter of 2–4 mm and fragments of plant fossils (Fig. 6A and B). It has a high sorting coefficient of 1.92 to 3.51 ϕ (averaging at 2.68 ϕ) (Table 2), exhibits a unimodal to bimodal grain-size distribution patterns (Fig. 8A), and show a subdivision of cumulative distribution plots

Table 1
Tabulation of five main seismic facies recognized in the studied canyon head and their corresponding cross-sectional seismic manifestations, plan-view seismic geomorphological characteristics, and sedimentological interpretations.

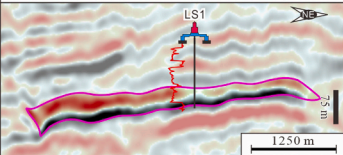
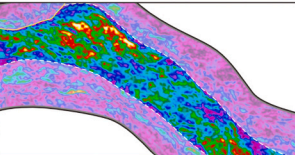
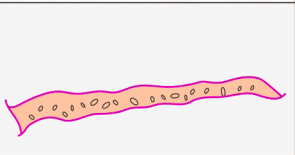
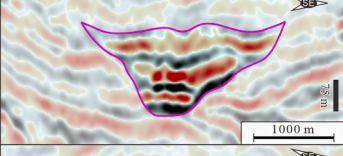
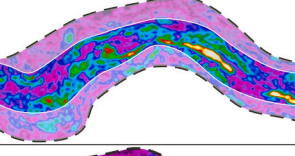

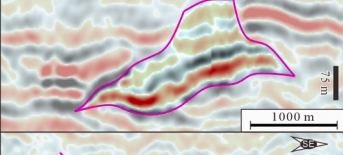
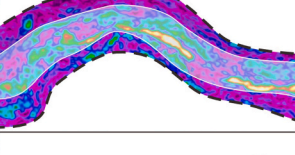
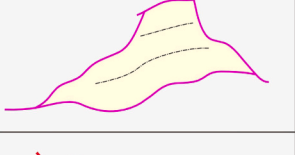
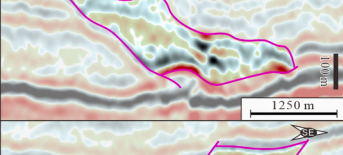
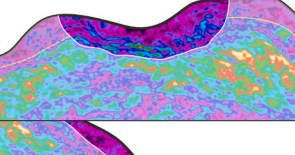

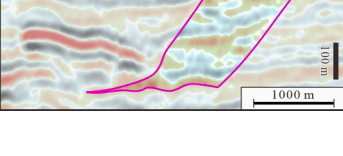
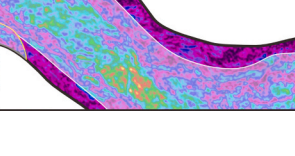

Seismic facies	Reflection configuration	Cross-sectional seismic expression			Cross-sectional seismic manifestations	Planform seismic geomorphology	Cross-sectional line drawings	Interpretation
		Amplitude	Continuity	Geometry				
Seismic facies 1	N/A	High	High	Lens or irregular				Thalweg sandy debrites
Seismic facies 2	Sub-parallel	High	Variable	Mounded, convex-up				Axial high net-to-gross turbidites
Seismic facies 3	Sub-parallel	Moderate to low	Variable	Irregular-shaped				Off-axial low net-to-gross turbidites
Seismic facies 4	Chaotic	Variable	Variable	Irregular-shaped				Bank failures
Seismic facies 5	Sub-parallel	Low	Moderate to low	Irregular-shaped				Internal levees

Table 2
Tabulation of grain-size compositions and sorting parameters of thalweg sandy debrites (lithofacies 1) and axial high net-to-gross turbidites (lithofacies 2 and 3).

Lithofacies	Depth (m)	N	Pebbles ($\varphi < 0$) (%)	Sand ($0 < \varphi < 4$) (%)	Silt ($4 < \varphi < 8$) (%)	Clay ($\varphi > 8$) (%)	σ_1 (φ)	Average
			range	range	range	range	range	
Lithofacies 1	4720.8–4742.4	3	0–12.18	41.92–55.54	28.17–42.51	10.49–16.29	1.92–3.51	2.68
Lithofacies 2	4684.2–4714.8	10	N/A	46.27–66.18	20.65–39.55	11.21–16.92	2.28–2.84	2.64
Lithofacies 3	4654.6–4665.6	6	N/A	20.77–52.36	36.61–62.69	9.59–16.54	1.92–2.29	2.05

into a coarser-grained fraction associated with saltation load and a finer-grained fraction transported wholly in suspension (i.e., one- to two-segment grain-size distribution patterns) (Fig. 8B). In cross-sectional view, this seismic facies appears immediately above the fifth-order or fourth-order erosion surfaces as a single high-amplitude, continuous trough reflector (red color) (Figs. 3 and 4; Table 1). In plan-view, seismic facies 1 is imaged as depositional dip-elongated, wide, tortuous high-RMS bands (Fig. 9A, B; Table 1).

Seismic facies 1 (thalweg sandy debrites) exhibits the evidence for the deposition of the early stage of canyon or channel formation, including its stratigraphic positions (Figs. 3, 4, and 6), the occurrence of sharp lithological contacts at their base (panel B in Fig. 8). The characteristics of massive structure, development of small pebbles (panels A and B in Fig. 8), and presence of one- to two-segment grain-size distribution and associated unimodal to bimodal grain-size distribution patterns (Fig. 10A and B) in its lithofacies (Lithofacies 1) suggest that it is probably the product of rapid deposition of debris flows (e.g., Shanmugam, 1996, 2012; Cartigny et al., 2014; Wang et al., 2024). We,

therefore, relate this seismic facies to thalweg deposits generated by sandy debris-flow during the early stage of channel formation (Figs. 3, 4, 6, 7A, B; Table 1) (Shanmugam, 1996, 2012; Mulder and Alexander, 2001).

(2) *Seismic facies 2 (mounded, middle-frequency and high amplitude reflections)* is characterized by blocky low gamma-ray patterns are recognized in well LS1 (Fig. 5), composed of 20 to 50 m thick medium- to fine-grained sandstones with mudstone intervals (Figs. 6 and 7), besides, three lithofacies (Lithofacies 2, 3 and 4) are recognized in the cores from LS1 (Figs. 6 and 7). Lithofacies 2 is made up of thick, structureless, medium to fine sandstones (reported as sand content of 46.27–66.18 %), and differentiate from lithofacies 1 with the lack of pebbles or plant fossils (Figs. 6C to 6E, and 7H). This lithofacies has a medium sorting coefficient ranging from 2.28 to 2.84 φ (averaging at 2.64 φ) (Table 2), and exhibits a bimodal grain-size distribution patterns (Fig. 8C) and a two-segment grain-size distribution patterns (Fig. 8D). *Lithofacies 3* comprises gray, fine-grained sandstones with widespread occurrence of different types of bedding such as

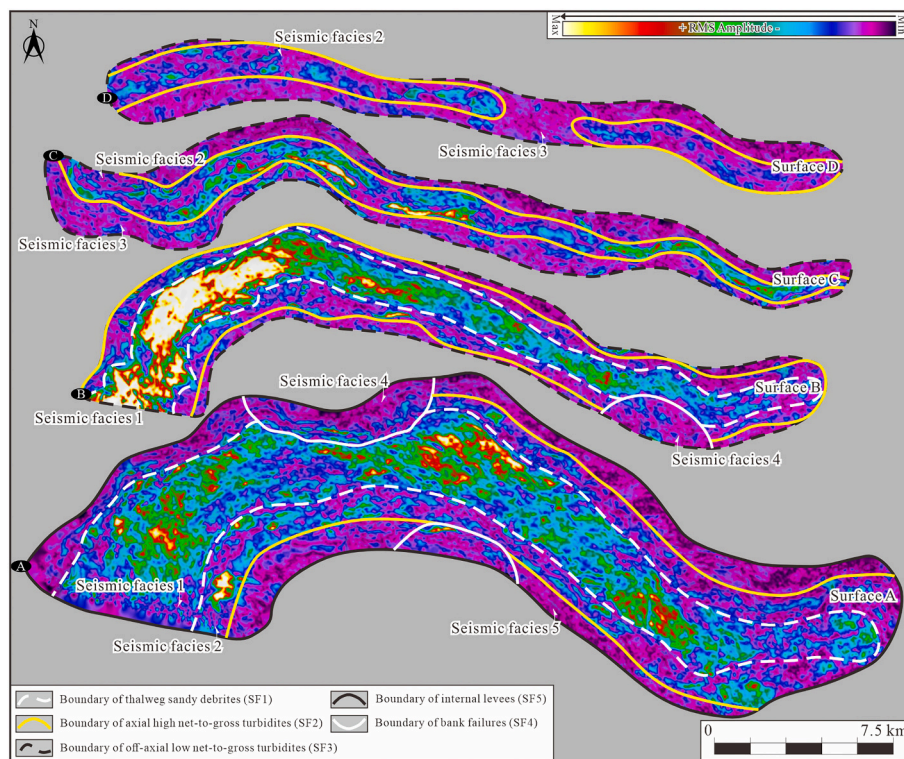


Fig. 9. RMS attribute maps taken 20 m above the fifth-order erosional surface (Surface A shown in Figs. 3 and 4) and fourth-order erosional surfaces (Surfaces B to D shown in Figs. 3 and 4) illustrating plan-view seismic geomorphological characteristics of thalweg sandy debrites, axial high net-to-gross turbidites, off-axial low net-to-gross turbidites, bank failures, and internal levees recognized in the trunk submarine canyon as documented in this study. SF: seismic facies.

parallel to low-angle bedding and wavy bedding (Fig. 7A, C to 7E, and 7G). This lithofacies has a low sorting coefficient of 1.92 to 2.29 ϕ (averaging at 2.05 ϕ) (Table 2), and also exhibits a bimodal grain-size distribution patterns (Fig. 8E) and a two-segment grain-size distribution patterns composed of a coarser-grained fraction transported in saltation load and a finer-grained fraction transported in suspension (Fig. 8F). *Lithofacies 4* is composed of dark gray, structureless mudstones with the occurrence of nodules and sandy clumps (Fig. 7B, F, and I).

In cross-sectional view, this seismic facies preferentially developed along the axial part of those erosion surfaces (Figs. 3 and 4). It is made up of vertically stacked, high amplitude, middle to low frequency, moderate continuous to chaotic seismic reflections with channel features, and displays an overall mounded, convex-up geometry (Figs. 3 and 4; Table 1). In the plan form, this seismic facies appears as depositional dip-elongated, narrow, tortuous high-RMS bands flanked by low RMS bands (Figs. 9C; Table 1).

Seismic facies 2 (axial high net-to-gross turbidites) exhibits similarities in cross-sectional geometry, characterized by a mounded, convex-upward morphology, and planform seismic geomorphology, defined by narrow, sinuous, high-RMS amplitude bands, consistent with sand-prone fills reported by Janocko et al. (2013) and stacked high net-to-gross channel axial deposits documented by Mayall et al. (2006) and Mayall and Kneller (2021). Among the recognized lithofacies, *lithofacies 2* is characterized by massive medium sandstones with an absence of fine pebbles and a low sorting coefficient, indicative of deposition from waning or quasi-steady, high-density turbidity currents with elevated sediment fallout rates (cf., Bouma et al., 1962; Lowe, 1982; Kneller and Branney, 1995; Talling et al., 2012; Cartigny et al., 2014; Li et al., 2016). These characteristics enable the correlation of *lithofacies 2* with high-density turbidity currents, resulting in massive sandstones comprising multiple, vertically stacked Bouma Ta divisions (i.e., high-density turbidites) (Figs. 6C, D, E, and 7H). *Lithofacies 3* is distinguished by a low

sorting coefficient, finer grain size, and the prevalent occurrence of varied bedding structures, collectively indicating deposition from low-density turbidity currents, resulting in low-density turbidites comprising Bouma Tb, Tc, and Td divisions (Bouma et al., 1962; Lowe, 1982; Gagnon and Waldron, 2011; Liu et al., 2016). *Lithofacies 4* is characterized by structureless mudstones, dark gray core coloration, and sedimentary features such as nodules and sandy clumps, which are consistent with deposition from dilute turbidity currents in deep-marine settings (mudstones formed by dilute turbidity currents) (Fig. 7B, F, and I) (Zavala et al., 2011; Henstra et al., 2016). The high net-to-gross ratio of this seismic facies (Fig. 5), coupled with the interpretation of those lithofacies, supports its interpretation as axial high net-to-gross turbidites (Figs. 3 to 5; Table 1) (Janocko et al., 2013; Li et al., 2016; Mayall and Kneller, 2021).

- (3) *Seismic facies 3 (subparallel, middle-frequency and moderate-to-low amplitude reflections)* appears immediately above the inner flanks of those recognized erosion surfaces (Figs. 3 and 4). In cross-sectional view, it is composed of moderate to low amplitude, discontinuous seismic reflections, and show characteristics of brighter, more semicontinuous than seismic facies 2 and generally without channel like features (Figs. 3 and 4; Table 1). In plan-view, seismic facies 3 is imaged as amorphous, moderate- to low-RMS accumulations, and contain more darker colored RMS patches than seismic facies 2 (Figs. 9B to 9D; Table 1).

Seismic facies 3 (off-axial low net-to-gross turbidites) is characterized by lower-amplitude reflectors and darker-colored RMS amplitude accumulations compared to axial high net-to-gross turbidites, occurring on their flanks (Figs. 3, 4, 9B to 9D), suggesting a facies transition from channel axis to channel margin. Seismic facies 3 can, therefore, be interpreted as off-axial low net-to-gross turbidites (Figs. 3 and 4; Table 1) (Mayall et al., 2006; Li et al., 2016; Mayall and Kneller, 2021).

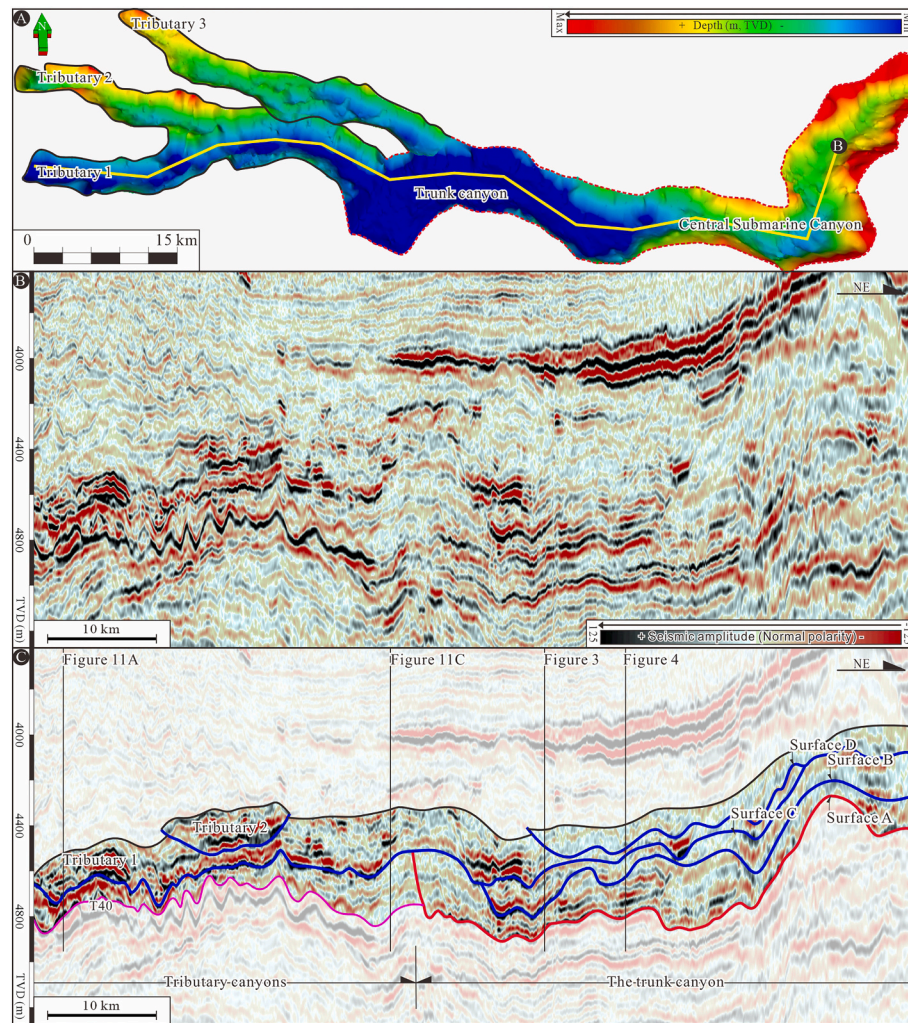


Fig. 10. (A) Three-dimensional perspective of depth structure diagram of the base of the studied canyon head illustrating plan-view morphology of the documented tributary and trunk submarine canyons. Also shown are plan-view locations of seismic lines shown in panels B and C. (B and C) Depositional dip-oriented seismic profile illustrating stratigraphic correlations and hierarchical relationships between tributary canyons expressed as fourth-order erosion surfaces and the trunk canyon composed of a fifth-order erosion surface and three fourth-order erosion surfaces. Note again that three tributary submarine canyons downstream converge into the trunk canyon. Surface A: fifth-order erosional surface (basal bounding surface of the trunk canyon); Surfaces B to D: fourth-order erosional surfaces.

(4) *Seismic facies 4 (chaotic reflections)* is adjacent to the fifth-order erosion surface, as its seismic reflectors are inclined toward canyon walls and downlap toward the canyon thalweg (Figs. 3 and 4). In section view, it is typified by moderate- to low-amplitude, chaotic-discontinuous, highly angled reflectors, and displays an overall irregular-shaped cross-sectional geometry (Figs. 3 and 4; Table 1). In the plan form, this seismic facies exhibits an amorphous morphology, and is represented by low-RMS accumulations with sporadic occurrence of high-RMS patches (Fig. 9A and B; Table 1).

Seismic facies 4 (bank failures) displays many of the recognition criteria typically utilized to identify mass-transported complexes (i.e., irregular-shaped, chaotic to discontinuous, highly angled reflectors) (e.g., Bull et al., 2009; Janocko et al., 2013; Kremer et al., 2018). Its stratigraphic positions adjacent to canyon walls suggest that it can be related to collapses and/or gravitational instabilities on canyon margins by high-energy sediment gravity flows operating within the studied canyon. As a result, we interpret the seismic facies 4 as bank failures (Figs. 3, 4, and 9A; Table 1).

(5) *Seismic facies 5 (wedge-shaped, middle-frequency and low amplitude reflections)* is dominated by thick mudstones with an upward decreasing trend in GR values (Fig. 5). It appears along both flanks of the fourth-order erosion surface, and is totally confined within the initial incisions (Figs. 3 and 4). In cross-sectional view, it is composed of semicontinuous to continuous, low-amplitude seismic reflections, and decreases in thickness away from the axis of the fourth-order erosion surface (Figs. 3 and 4; Table 1). In plan-view, this seismic facies is imaged on RMS amplitude maps as low-RMS accumulations (Fig. 9A; Table 1).

Seismic facies 5 (internal levees) occurs adjacent to fourth-order erosion surfaces and surrounded by the fifth-order erosion surface, suggesting that it was most likely formed by overspilling and delivering fine-grained sediments onto overbank environments when submarine channel turbidity currents exceed the confinement height of the erosion surfaces (e.g., Hansen et al., 2015, 2017; Deptuck and Sylvester, 2017). This interpretation is further supported by its low net-to-gross ratio characters and the upward-coarsening pattern showing in GR logs (Fig. 5A). It is confined totally within the initial incisions has been referred to as “internal levees” (Figs. 3, 4, and 9A; Table 1).

5. Discussion

5.1. Differences between trunk versus tributary canyons

As shown in the depth-domain structural map of the documented canyon head, three tributary canyons (tributary 1, 2 and 3) downstream merge with, and converge into the trunk canyon (Fig. 10A), which is also documented in the depositional dip-oriented seismic profile (Fig. 10B and C). A comparison in hierarchies between trunk versus tributary canyons suggests that the trunk canyon is characterized by the presence of two types of stratigraphic surfaces, a larger morphology, and by a higher hierarchical level (Figs. 3 and 4). Whereas tributary canyons are characterized by a lack of the fifth-order erosion surfaces, a smaller morphology, and by a lower hierarchical level (Figs. 10 and 11). The trunk canyon is characterized by a more complex depositional style (Figs. 3 and 4 versus 11), containing five main depositional facies, and are composed of multiple laterally migrated and vertically nested fining-upward facies successions, each of which comprises thalweg sandy debrites in the lower part, grading upward into axial high net-to-gross turbidites or off-axial low net-to-gross turbidites and, finally, into bank failures or internal levees (Figs. 3, 4 and 5). Tributary canyons, in marked contrast, are characterized by vertical stacked pattern with the lack of internal levees, and consist of a single fining-upward facies succession (Fig. 11). This demonstrates that the trunk canyon went

through multiple phases of canyon cut, fill and abandonment, while tributary canyons were buried after one phase (e.g., McArthur and McCaffrey, 2019).

5.2. Evolution of the tributary and trunk canyons

Evolution of the tributary and trunk canyons recognized in the Central Submarine Canyon head are summarized, as shown in the regional RMS attribute maps and their corresponding interpretations (Figs. 12 and 13). The trunk canyon developed firstly, fostered more sandy depositional architectures comprising thalweg sandy debrites, axial high net-to-gross turbidites and some off-axial low net-to-gross turbidites (Fig. 12). While, less muddy depositional architectures developed during this stage, only several bank failures were locally recognized (Fig. 12). This suggests that gravity flows were frequent and transported substantial volumes of sediment during this stage (Maier et al., 2018).

Three nearly east-west oriented tributary canyons formed and downstream converge into the trunk canyon, evolving in a tree branch-like network in the second stage (Figs. 10A and 13). Sandy depositional architectures mainly developed in the tributary canyons (i.e., thalweg sandy debrites, axial high net-to-gross turbidites and off-axial low net-to-gross turbidites), while muddy depositional architectures (internal levees) are widely recognized in the trunk canyon (Fig. 13). This may

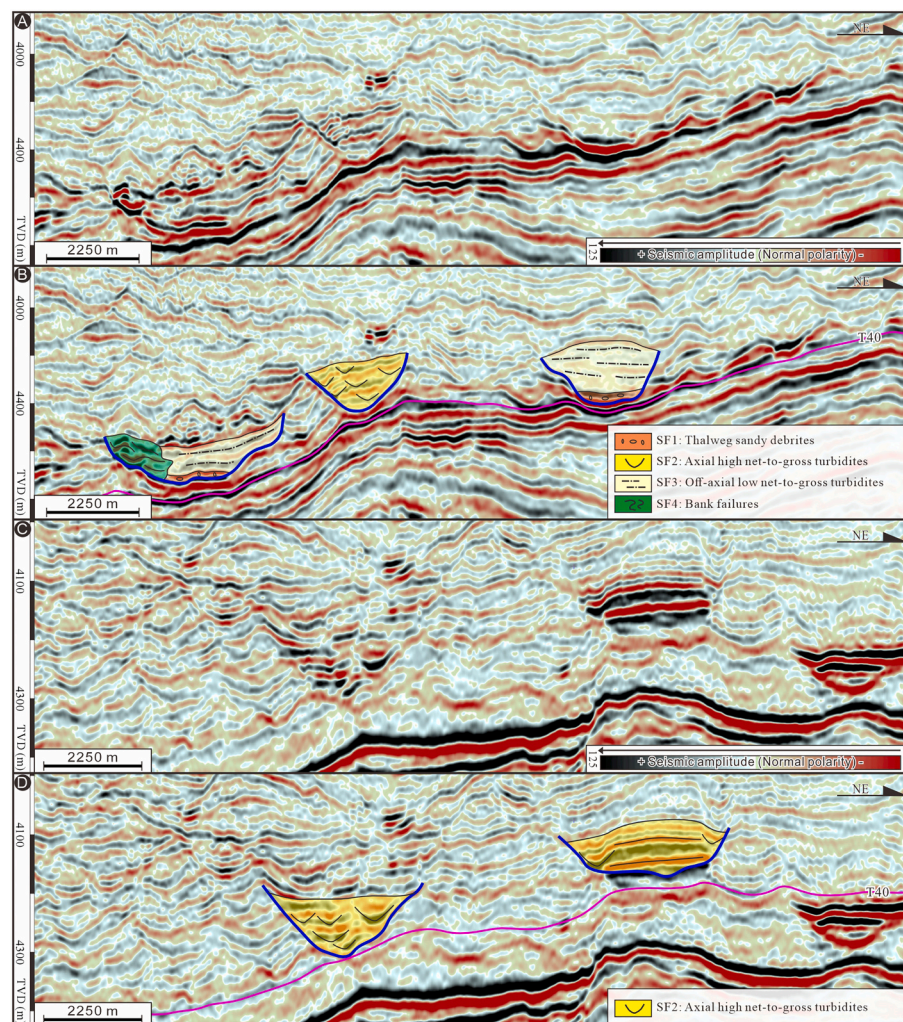


Fig. 11. Depositional strike-view seismic traverse across the studied submarine canyons (see its plan-view location in Fig. 1B) and corresponding sedimentological interpretations illustrating hierarchies and architectures of tributary canyons. Note that each tributary canyon contains only a fourth-order erosional surface, less depositional facies, and lack internal levees. SF: seismic facies.

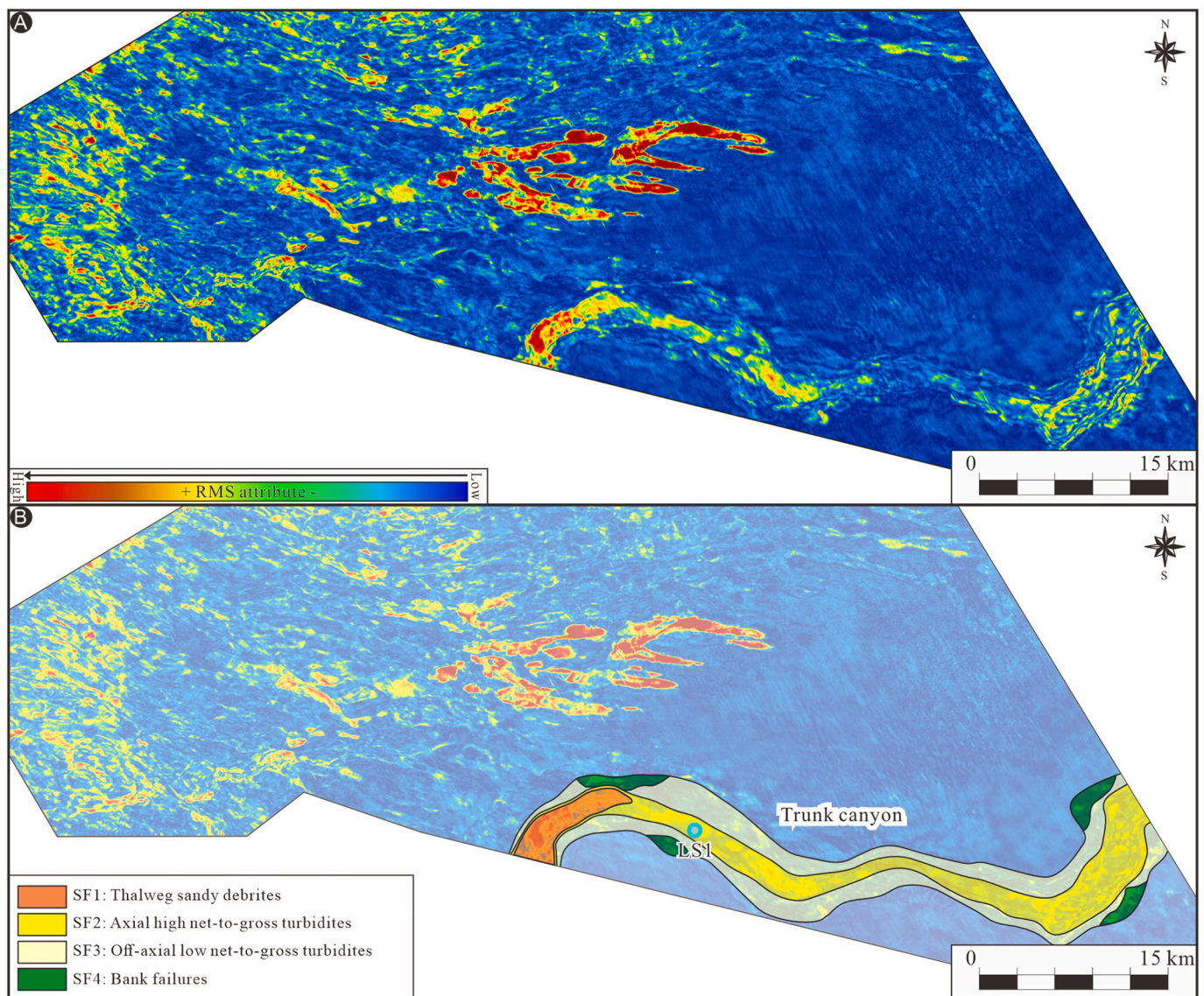


Fig. 12. (A) Representative RMS amplitude attribute map (see its plan-view location in Fig. 1B) taken 40 m above the base of late Miocene Huangliu Formation (T40) and (B) its interpretation illustrating geomorphological expressions of the development of the canyon head and its internal architectures during the first stage. Note that no tributary canyons developed during this stage.

attribute to a decrease in energy and volume of gravity flows (Cronin et al., 2005; Bernhardt et al., 2015; McArthur and McCaffrey, 2019), as those erosional surfaces developed in this stage are narrower and shallower (Surfaces C and D shown in Figs. 3 and 4), and sandy depositional architectures mainly developed in tributary canyons (Fig. 13). Similar infill characteristics have also been reported in other submarine canyons (e.g., Cronin et al., 2005; Mountjoy et al., 2009).

During the second stage, tributary canyons initiated later than the trunk canyon, as evidenced by the trunk canyon cut through the basal bounding surface (T40) while the tributary canyons do not (Figs. 3, 4, and 11); the depth of basal surfaces of tributary canyons are higher than the basal bounding surface of the trunk canyon (Fig. 10A). Considering the paleotopography of the Qiongdongnan Basin, which gradually deepens from west to east (Xie et al., 2008; Chen et al., 2015; Zhao et al., 2018). It is inferred that this development process resulted from the tributary canyons eroding downstream and merging into the early-formed trunk canyon (Figs. 1B and 13), which is in agreement with the mechanism suggested by Shepard (1981), Pratson et al. (1994) and Pratson and Coakley (1996).

5.3. Implications

As a representative type of submarine canyon head, dendritic submarine canyon head has been well documented in terms of its distinctive geomorphic characteristics, as well as its geomorphic variations of tributary and the trunk canyons (García et al., 2006; Tubau et al., 2013; Bernhardt et al., 2015; Puig et al., 2017), whereas describing the sedimentary infillings and their variations from the tributary to trunk canyons remain few reported (Cronin et al., 2005; Gamberi et al., 2017; Maier et al., 2018). Observations and results derived from the present study highlight the depositional architectures and corresponding evolution of the dendritic submarine canyon head, reveal the variation of the hierarchical framework and architectural properties that distinguish the tributary canyons from the trunk canyon, therefore, these insights contributing to a better understanding of the sedimentary architectures and evolution of dendritic submarine canyon head.

6. Conclusions

High-resolution 3-D seismic data tied to well-log, core, and grain-size

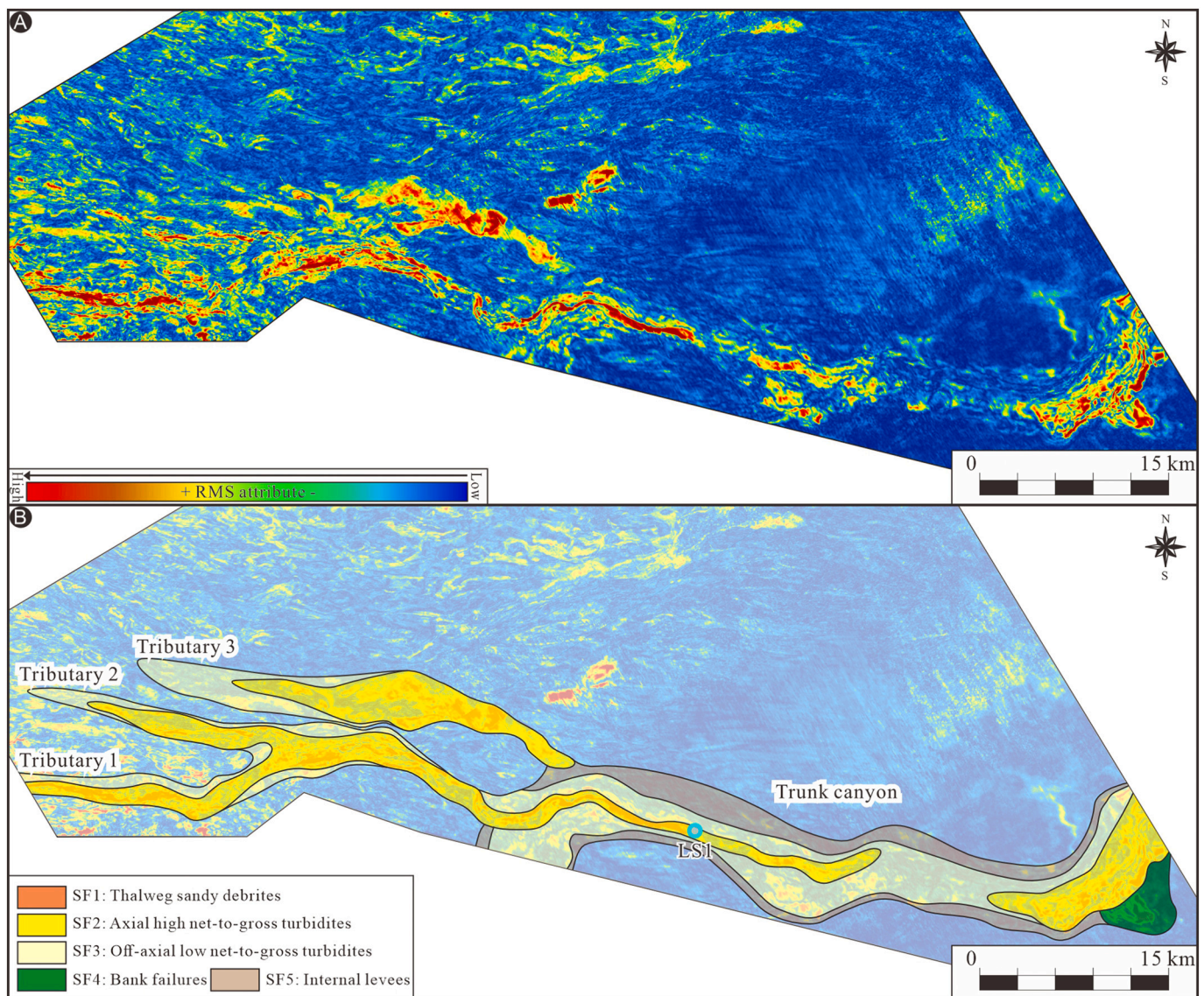


Fig. 13. (A) Representative RMS amplitude attribute map (see its plan-view location in Fig. 1B) taken 160 m above the base of late Miocene Huangliu Formation (T40) and (B) its interpretation illustrating geomorphological expressions of the development of the canyon head and its internal architectures during the second stage. Note that three tributary submarine canyons oriented from the northwest downstream converge into the trunk canyon.

data from the head of Central Submarine Canyon in late Miocene Qiongdongnan Basin are utilized to investigate the variations of hierarchies and architectures between trunk versus tributary canyons, and their evolution.

Two types of stratigraphic surfaces and five types of depositional elements including thalweg sandy debrites, axial high net-to-gross turbidites, off-axial low net-to-gross turbidites, bank failures, and internal levees are recognized in the studied trunk and tributary canyons within the canyon head region. Among them, thalweg sandy debrites are composed of massive coarse sandstones with pebbles, axial high net-to-gross turbidites mainly consist of structureless coarse sandstones and fine-grained sandstones with various bedding, both of which are most sand-rich sedimentary facies in the canyon head.

The comparison of the documented trunk and tributary canyons suggests that the trunk canyon is distinguished from tributary canyons by a more complex depositional style expressed as the occurrence of internal levees and multiple fining-upward facies successions.

The studied canyon head evolved through two stages, an early stage with only the development of the trunk canyon, followed by a later stage in which three individual tributary canyons downstream converged into

the trunk canyon to form a dendritic canyon head. This evolutionary process is the result of downstream erosion by tributary canyons under the control of paleo-topography.

CRediT authorship contribution statement

Dongwei Li: Writing – original draft, Investigation, Formal analysis, Conceptualization. **Chenglin Gong:** Writing – review & editing, Supervision, Project administration, Formal analysis. **Ronald J. Steel:** Writing – review & editing. **Yijie Zhu:** Validation, Software, Methodology.

Declaration of competing interest

The authors declare that they have no known competing financial interests or personal relationships that can influence the work reported in this paper.

Acknowledgments

We are grateful to Giorgio Basilici (editor-in-chief), Ben Kneller and two anonymous reviewers for taking the time to go through the manuscript for their critical but constructive comments, all of which significantly improved the overall quality of this paper. We gratefully thank CNOOC Hainan Branch Company for providing and permitting publishing the subsurface data, and acknowledge financial support from the program of China Scholarship Council (No. 202406440100).

Data availability

Access to the raw data would require approval by CNOOC Hainan Branch Company.

Data availability

Access to the raw data would require approval by CNOOC Hainan Branch Company.

References

- Anderson, K.S., Graham, S.A., Hubbard, S.M., 2006. Facies, architecture, and origin of a reservoir-scale sand-rich succession within submarine canyon fill: insights from Wagon Caves Rock (Paleocene), Santa Lucia Range, California, USA. *Journal of Sedimentary Research* 76 (5), 819–838.
- Babonneau, N., Savoye, B., Cremer, M., Klein, B., 2002. Morphology and architecture of the present canyon and channel system of the Zaire deep-sea fan. *Marine and Petroleum Geology* 19, 445–467.
- Baker, M.L., Hage, S., Talling, P.J., Acikalin, S., Hilton, R.G., Haghpor, N., Ruffell, S.C., Pope, E.L., Jacinto, R.S., Clare, M.A., Sahin, S., 2024. Globally significant mass of terrestrial organic carbon efficiently transported by canyon-flushing turbidity currents. *Geology* 52 (8), 631–636.
- Bernhardt, A., Schwanghart, W., 2025. Seafloor slopes control submarine canyon distribution: a global analysis. *Science Advances* 11 (24), eadv3942.
- Bernhardt, A., Melnick, D., Jara-Muñoz, J., Argandoña, B., González, J., Strecker, M.R., 2015. Controls on submarine canyon activity during sea-level highstands: the Biobío canyon system offshore Chile. *Geosphere* 11 (4), 1226–1255.
- Bouma, A.H., Kuenen, P.H., Shepard, F.P., 1962. *Sedimentology of some Flysch Deposits: a Graphic Approach to Facies Interpretation*.
- Bruno, L., Amorosi, A., Lugli, S., Sammartino, I., Fontana, D., 2021. Trunk river and tributary interactions recorded in the Pleistocene–Holocene stratigraphy of the Po Plain (northern Italy). *Sedimentology* 68 (6), 2918–2943.
- Bull, S., Cartwright, J., Huuse, M., 2009. A review of kinematic indicators from mass-transport complexes using 3D seismic data. *Marine and Petroleum Geology* 26, 1132e1151.
- Cartigny, M.J., Ventra, D., Postma, G., van Den Berg, J.H., 2014. Morphodynamics and sedimentary structures of bedforms under supercritical-flow conditions: new insights from flume experiments. *Sedimentology* 61 (3), 712–748.
- Chen, H., Xie, X., Guo, J., Su, M., Zong, K., Shang, F., Huang, W., Wang, W., Shang, Z., 2015. Provenance of Central Canyon in Qiongdongnan Basin as evidenced by detrital zircon U-Pb study of Upper Miocene sandstones. *Science China Earth Sciences* 58 (8), 1337–1349.
- Chopra, S., Marfurt, K.J., 2007. *Seismic Attributes for Prospect Identification and Reservoir Characterization*. Society of Exploration Geophysicists and European Association of Geoscientists and Engineers.
- Cronin, B.T., Akhmetzhanov, A.M., Mazzini, A., Akhmanov, G., Ivanov, M., Kenyon, N. H., 2005. Morphology, evolution and fill: implications for sand and mud distribution in filling deep-water canyons and slope channel complexes. *Sedimentary Geology* 179 (1–2), 71–97.
- Deptuck, M.E., Sylvester, Z., 2017. *Submarine fans and their channels, levees, and lobes*. In: *Submarine geomorphology*. Springer International Publishing, Cham, pp. 273–299.
- Di Celma, C., 2011. Sedimentology, architecture, and depositional evolution of a coarse-grained submarine canyon fill from the Gelasian (early Pleistocene) of the Peri-Adriatic basin, Offida, Central Italy. *Sedimentary Geology* 238 (3–4), 233–253.
- Di Celma, C., Cantalamessa, G., Didaskalou, P., Lori, P., 2010. Sedimentology, architecture, and sequence stratigraphy of coarse-grained, submarine canyon fills from the Pleistocene (Gelasian-Calabrian) of the Peri-Adriatic basin, Central Italy. *Marine and Petroleum Geology* 27 (7), 1340–1365.
- Fildani, A., 2017. Submarine canyons: a brief review looking forward. *Geology* 45 (4), 383–384.
- Flint, S.A., Hodgson, D.M., Sprague, A.R., Brunt, R.L., Van der Merwe, W.C., Figueiredo, J., Prêlat, A., Box, D., Di Celma, C., Kavanagh, J.P., 2011. Depositional architecture and sequence stratigraphy of the Karoo basin floor to shelf edge succession, Laingsburg depocentre, South Africa. *Marine and Petroleum Geology* 28 (3), 658–674.
- Gagnon, J.F., Waldron, J.W., 2011. Sedimentation styles and depositional processes in a Middle to late Jurassic slope environment, Bowser Basin, northwestern British Columbia. *Canada. Marine and Petroleum Geology* 28 (3), 698–715.
- Galy, V., France-Lanord, C., Beyssac, O., Faure, P., Kudrass, H., Palhol, F., 2007. Efficient organic carbon burial in the Bengal fan sustained by the Himalayan erosional system. *Nature* 450, 407–410.
- Gamberi, F., Breda, A., Mellere, D., 2017. Depositional canyon heads at the edge of narrow and tectonically steepened continental shelves: comparing geomorphic elements, processes and facies in modern and outcrop examples. *Marine and Petroleum Geology* 87, 157–170.
- García, M., Alonso, B., Ercilla, G., Gràcia, E., 2006. The tributary valley systems of the Almería Canyon (Alboran Sea, SW Mediterranean): sedimentary architecture. *Marine Geology* 226 (3–4), 207–223.
- Ghosh, B., Lowe, D.R., 1993. The architecture of Deepwater channel complexes, cretaceous Venado Sandstone Member, Sacramento Valley, California. Pacific Section, Guidebook 73. In: Graham, S.A., Lowe, D.R. (Eds.), *Advances in the Sedimentary Geology of the Great Valley Group*. SEPM, Sacramento Valley, California, p. 51e65.
- Gong, C., Wang, Y., Zhu, W., Li, W., Xu, Q., Zhang, J., 2011. The Central Submarine Canyon in the Qiongdongnan Basin, northwestern South China Sea: architecture, sequence stratigraphy, and depositional processes. *Marine and Petroleum Geology* 28 (9), 1690–1702.
- Gong, C., Steel, R.J., Qi, K., Wang, Y., 2021. Deep-water channel morphologies, architectures, and population densities in relation to stacking trajectories and climate states. *GSA Bulletin* 133 (1–2), 287–306.
- Hansen, L., Janocko, M., Kane, I., Kneller, B., 2017. Submarine channel evolution, terrace development, and preservation of intra-channel thin-bedded turbidites: Mahin and Avon Channels, offshore Nigeria. *Marine Geology* 383, 146–167.
- Hansen, L.A.S., Callow, R.H.T., Kane, I.A., Gamberi, F., Rovere, M., Cronin, B.T., Kneller, B.C., 2015. Genesis and character of thin-bedded turbidites associated with submarine channels. *Marine and Petroleum Geology* 67, 852–879.
- Harris, P.T., Whiteway, T., 2011. Global distribution of large submarine canyons: Geomorphic differences between active and passive continental margins. *Marine Geology* 285 (1–4), 69–86.
- Harris, P.T., Macmillan-Lawler, M., Rupp, J., Baker, E.K., 2014. Geomorphology of the oceans. *Marine Geology* 352, 4–24.
- Henstra, G.A., Grundvåg, S.A., Johannessen, E.P., Kristensen, T.B., Midtkandal, I., Nystuen, J.P., Windelstad, J., 2016. Depositional processes and stratigraphic architecture within a coarse-grained rift-margin turbidite system: the Wollaston Forland Group, East Greenland. *Marine and Petroleum Geology* 76, 187–209.
- Huang, B., Tian, H., Li, X., Wang, Z., Xiao, X., 2016. Geochemistry, origin and accumulation of natural gases in the Deepwater area of the Qiongdongnan Basin, South China Sea. *Marine and Petroleum Geology* 72, 254–267.
- Janocko, M., Nemec, W., Henriksen, S., Warchol, M., 2013. The diversity of deep-water sinuous channel belts and slope valley-fill complexes. *Marine and Petroleum Geology* 41, 7–34.
- Klaucke, I., Hesse, R., Ryan, W.B., 1998. Morphology and structure of a distal submarine trunk channel: the Northwest Atlantic Mid-Ocean Channel between lat 53°N and 44°30'N. *Geological Society of America Bulletin* 110 (1), 22–34.
- Kneller, B.C., Branney, M.J., 1995. Sustained high-density turbidity currents and the deposition of thick massive sands. *Sedimentology* 42 (4), 607–616.
- Kremer, C.H., McHargue, T., Scheucher, L., Graham, S.A., 2018. Transversely-sourced mass-transport deposits and stratigraphic evolution of a foreland submarine channel system: Deep-water tertiary strata of the Austrian Molasse Basin. *Marine and Petroleum Geology* 92, 1–19.
- Li, P., Kneller, B.C., Hansen, L., Kane, I.A., 2016. The classical turbidite outcrop at San Clemente, California revisited: an example of sandy submarine channels with asymmetric facies architecture. *Sedimentary Geology* 346, 1–16.
- Liu, F., Zhu, X., Li, Y., Xue, M., Sun, J., 2016. Sedimentary facies analysis and depositional model of gravity-flow deposits of the Yanchang Formation, southwestern Ordos Basin, NW China. *Australian Journal of Earth Sciences* 63 (7), 885–902.
- Lowe, D.R., 1982. Depositional models with special reference to the deposits of high-density turbidity currents. *Journal of Sedimentary Petrology* 52 (1), 279–297.
- Maier, K.L., Johnson, S.Y., Hart, P., 2018. Controls on submarine canyon head evolution: Monterey Canyon, offshore Central California. *Marine Geology* 404, 24–40.
- Mayall, M., Kneller, B., 2021. Seismic interpretation workflows for deep-water systems: a practical guide for the subsurface. *AAPG Bulletin* 105 (11), 2127–2157.
- Mayall, M., Jones, E., Casey, M., 2006. Turbidite channel reservoirs—Key elements in facies prediction and effective development. *Marine and Petroleum Geology* 23 (8), 821–841.
- McArthur, A.D., McCaffrey, W.D., 2019. Sedimentary architecture of detached deep-marine canyons: examples from the East Coast Basin of New Zealand. *Sedimentology* 66 (3), 1067–1101.
- Morley, C.K., 2016. Major unconformities/termination of extension events and associated surfaces in the South China Seas: Review and implications for tectonic development. *Journal of Asian Earth Sciences* 120, 62–86.
- Mountjoy, J.J., Barnes, P.M., Pettinga, J.R., 2009. Morphostructure and evolution of submarine canyons across an active margin: Cook Strait sector of the Hikurangi margin, New Zealand. *Marine Geology* 260 (1–4), 45–68.
- Mulder, T., Alexander, J., 2001. The physical character of subaqueous sedimentary density-flows and their deposits. *Sedimentology* 48 (2), 269–299.
- Normark, W.R., Carlson, P.R., 2003. Giant Submarine Canyons: Is Size any Clue to their Importance in the Rock Record?.

- Pratson, L.F., Coakley, B.J., 1996. A model for the headward erosion of submarine canyons induced by downslope-eroding sediment flows. *Geological Society of America Bulletin* 108 (2), 225–234.
- Pratson, L.F., Ryan, W.B., Mountain, G.S., Twichell, D.C., 1994. Submarine canyon initiation by downslope-eroding sediment flows: evidence in late Cenozoic strata on the New Jersey continental slope. *Geological Society of America Bulletin* 106 (3), 395–412.
- Puig, P., Palanques, A., Martín, J., 2014. Contemporary sediment-transport processes in submarine canyons. *Annual Review of Marine Science* 6 (1), 53–77.
- Puig, P., Durán, R., Muñoz, A., Elvira, E., Guillén, J., 2017. Submarine canyon-head morphologies and inferred sediment transport processes in the Alfas-Almanzora canyon system (SW Mediterranean): on the role of the sediment supply. *Marine Geology* 393, 21–34.
- Shanmugam, G., 1996. High-density turbidity currents; are they sandy debris flows? *Journal of Sedimentary Research* 66 (1), 2–10.
- Shanmugam, G., 2012. New perspectives on deep-water sandstones: Origin, recognition, initiation, and reservoir quality. In: *Handbook of petroleum exploration and production*, v. 9. Elsevier, Amsterdam, pp. 67–127.
- Shepard, F.P., 1981. Submarine canyons: multiple causes and long-time persistence. *AAPG Bulletin* 65 (6), 1062–1077.
- Smith, M.E., Werner, S.H., Buscombe, D., Finnegan, N.J., Sumner, E.J., Mueller, E.R., 2018. Seeking the shore: evidence for active submarine canyon head incision due to coarse sediment supply and focusing of wave energy. *Geophysical Research Letters* 45 (22), 12–403.
- Sprague, A.R., Sullivan, M.D., Campion, K.M., Jensen, G.N., Goulding, D.K., Sickafoose, D.K., Jennette, D.C., 2002. The physical stratigraphy of deep-water strata: a hierarchical approach to the analysis of genetically related elements for improved reservoir prediction. In: *American Association of Petroleum Geologists Annual Meeting Abstracts*, pp. 10–13. Houston, Texas.
- Sprague, A.R.G., Garfield, T.R., Goulding, F.J., Beaubouef, R.T., Sullivan, M.D., Rossen, C., Mellere, D., 2005. Integrated slope channel depositional models: the key to successful prediction of reservoir presence and quality in offshore West Africa. *CIPM, cuarto E-Exitep*, p. 1e13.
- Sun, R., Yao, X., Wang, X., Wu, K., Han, Y., Xu, J., Song, Z., 2022. Source-to-sink system and sedimentary characteristics of the lower Miocene submarine fans in the eastern Deepwater area of the Qiongdongnan Basin, northern South China Sea. *Frontiers in Earth Science* 10, 956594.
- Talling, P.J., Masson, D.G., Sumner, E.J., Malgesini, G., 2012. Subaqueous sediment density flows: Depositional processes and deposit types. *Sedimentology* 59 (7), 1937–2003.
- Tubau, X., Lastras, G., Canals, M., Micallef, A., Amblas, D., 2013. Significance of the fine drainage pattern for submarine canyon evolution: The Foix Canyon System, Northwestern Mediterranean Sea. *Geomorphology* 184, 20–37.
- Wang, J., La Croix, A.D., Wang, H., Pang, X., Liu, B., 2024. Flume experiments of gravity flows: Transformation from sandy debris flows to turbidity currents with clay matrix separation. *Sedimentary Geology* 461, 106576.
- Wonham, J.P., Jayr, S., Mougamba, R., Chuilon, P., 2000. 3D sedimentary evolution of a canyon fill (lower Miocene-age) from the Mandorove Formation, offshore Gabon. *Marine and Petroleum Geology* 17 (2), 175–197.
- Xie, X., Müller, R.D., Ren, J., Jiang, T., Zhang, C., 2008. Stratigraphic architecture and evolution of the continental slope system in offshore Hainan, northern South China Sea. *Marine Geology* 247 (3–4), 129–144.
- Yang, G., Yin, H., Gan, J., Wang, W., Zhu, J., Jia, D., Xiong, X., Xu, W., 2024. Structural segmentation in the Qiongdongnan Basin, South China Sea: insights from analog models and implications for hydrocarbon exploration. *AAPG Bulletin* 108 (5), 907–941.
- Zavala, C., Arcuri, M., Di Meglio, M., Diaz, H.G., Contreras, C., 2011. A Genetic Facies Tract for the Analysis of Sustained Hyperpycnal Flow Deposits.
- Zhao, Z., Sun, Z., Sun, L., Wang, Z., Sun, Z., 2018. Cenozoic tectonic subsidence in the Qiongdongnan basin, northern South China Sea. *Basin Research* 30, 269–288.